Research paper

Vibration-based elastic parameter identification of the diploë and cortical tables in dry cranial bones

E. Kohtanen [a,*], M. Mazzotti [b], M. Ruzzene [b], A. Erturk [a]

[a] G. W. Woodruff School of Mechanical Engineering, Georgia Institute of Technology, 771 Ferst Dr NW, Atlanta, GA 30332, USA
[b] P. M. Rady Department of Mechanical Engineering, University of Colorado Boulder, 1111 Engineering Dr, Boulder, CO 80309, USA

ARTICLE INFO

ABSTRACT

Various human skull models feature a layered cranial structure composed of homogeneous cortical tables and the inner diploë. However, there is a lack of fundamental validation work of such three-layer cranial bone models by combining high-fidelity computational modeling and rigorous experiments. Here, non-contact vibration experiments are conducted on an assortment of dry bone segments from the largest cranial bone regions (parietal, frontal, occipital, and temporal) to estimate the first handful of modal frequencies and damping ratios, as well as mode shapes, in the audio frequency regime. Numerical models that consider the cortical tables and the diploë as domains with separate isotropic material properties are constructed for each bone segment using a routine that identifies the cortical table–diploë boundaries from micro-computed tomography scan images, and reconstructs a three-dimensional geometry layer by layer. The material properties for cortical tables and diploë are obtained using a Hounsfield Unit-based mass density calculation combined with a parameter identification scheme for Young's modulus estimation. With the identified parameters, the average error between experimental and numerical modal frequencies is 1.3% and the modal assurance criterion values for most modes are above 0.90, indicating that the layered model is suitable for predicting the vibrational behavior of cranial bone. The proposed layered modeling and identified elastic parameters are also useful to support computational modeling of cranial guided waves and mode conversion in medical ultrasound. Additionally, the diploë elastic properties are rarely reported in the literature, making this work a fundamental characterization effort that can guide in the selection of material properties for human head models that consider layered cranial bone.

1. Introduction

The existing literature on the human skull and head vibration began forming in the 1950s–70s. Most investigations to date are framed in the broad context of better understanding human head injuries or bone-conducted sound. The first experimental studies focused on mechanical impedance (Franke, 1956; Hodgson et al., 1967; Stalnaker et al., 1971), some of which included limited vibration modeling. Khalil and Viano (Khalil et al., 1979) were the first to identify the dry skull mode shapes, finding significant differences from one skull to another. These differences were attributed to high variance in relative size between skull bones, bone thickness, material properties, suture characteristics, among other factors that are unique to individual skulls. Since then, there have been a handful of experimental works reporting mode shapes of skull bone (McKnight et al., 2013; Horácek et al., 2003; Eslaminejad et al., 2020). Other remarkable experimental research such as that conducted by Håkansson et al. (1994) have identified *in vivo*

resonance frequencies and damping coefficients in human heads with pre-existing titanium implants. Experimental vibration studies on *in vivo* human heads are relatively rare, likely due to the difficulty and cost of performing such experiments, while the scarcity for dry cranial bone studies can be explained in part by lack of direct applicability of such results to topics like hearing by bone conduction.

On the modeling side, many early papers employed elastic fluid-coupled spherical shell models (Engin, 1969; Hickling and Wenner, 1973), and similar idealized models have also been used more recently (El Baroudi et al., 2012; Charalambopoulos et al., 1997). However, due to the geometric and mechanical complexities involved, numerical models have mainly been developed using the finite element method (FEM), with the paper by Nickell and Marcal (1974) being one of the pioneering studies specifically devoted to the study of skull vibrations. The gradual development in FEM head models used in injury investigations has been described in Voo et al. (1996) and more

---

recently in Tse et al. (2017). High-fidelity numerical models of the human skull and brain can be obtained from computed tomography (CT) scans. This approach is used for example to compute natural frequencies and mode shapes in Tse et al. (2015) through a model that also features cerebrospinal fluid, nasal cartilage, and vertebrae.

Studies on traumatic brain injury due to blunt impacts have demonstrated that fundamental brain damage is associated with low frequency dynamics near 30 Hz (Laksari et al., 2018). For the purpose of these investigations, the distinction between single- or multi-layer descriptions of the skull bone, and even the assumption of rigid versus elastic bone are likely inconsequential. In contrast, for investigations of phenomena that involve higher frequencies such as blast-induced traumatic brain injury (Cotton et al., 2016) and bone conduction of sound, the detailed modeling of the layered bone structure is highly relevant. There are a number of works (Kleiven and von Holst, 2002; Kang et al., 1997; Sahoo et al., 2013) that consider a skull model with separate cortical table and diploë properties. The model in Chang et al. (2016) is particularly precise in its diploë geometry that is extracted from cryogenic images. However, the diploë properties have not been rigorously analyzed until quite recently, with significant efforts made into characterizing the layered cranial bone geometry (Alexander et al., 2019) and the layer material properties (Alexander et al., 2020) of fresh parietal and frontal bone. The latter paper, to our best knowledge, is the first to report distinct material properties for the cortical tables and the diploë in fresh cranial bone, although the results are limited to parietal and frontal bone.

This paper serves as a fundamental high-fidelity modeling and validation work for cranial bone vibration with a layered model. In addition, the vibration properties, quantified by modal parameters, are employed to extract material properties for the cortical tables and the diploë. To this end, a novel model construction process is employed to formulate FEM models where cranial bone segments are divided into their constituent layers, i.e. the outer cortical table, the diploë, and the inner cortical table. Five such models are generated for bone segments extracted from the parietal, frontal, occipital, and temporal bones of an 87-year-old dry male skull as seen in Fig. 1. It should be noted that while a statistical treatment is beyond the scope of this paper, the extracted diploë elastic moduli serve as some of the only available points of reference in the literature. The numerical models employ elastic properties obtained using a parameter identification scheme that seeks to minimize the difference between the numerical modal frequencies and those obtained from non-contact experimental vibration studies. The main contributions offered by this paper are twofold: (1) development of a procedure that allows for the formulation of a 3-layered cranial bone model from CT scan data, and (2) evaluation of equivalent elastic properties of the skull through vibration experiments, which also serve as validation of the developed models. While there are a number of complex human head models that use three layer skull models, there is no fundamental experimental and numerical validation work for the use of such cranial bone. This paper seeks to fill this void in the literature. Additionally, such layered modeling and identified elastic parameters are required to support computational models of cranial guided waves and mode conversion for medical ultrasound (Mazzotti et al., 2021a; Kohtanen et al., 2021a,b) (given the bone porosity and layeredness become more critical with shorter wavelengths at ultrasonic frequencies).

2. Layered geometry reconstruction

The cranial bone is in general separated into three layers: the inner and outer cortical tables, and the diploë, which has considerably different material properties than those of the cortical tables. With this natural distinction in mind, it is intuitive to consider a layered model in which the inner core and the adjacent regions employ different sets of material properties. To this end, a numerical model that faithfully represents the boundaries between the bone layers is constructed. First,
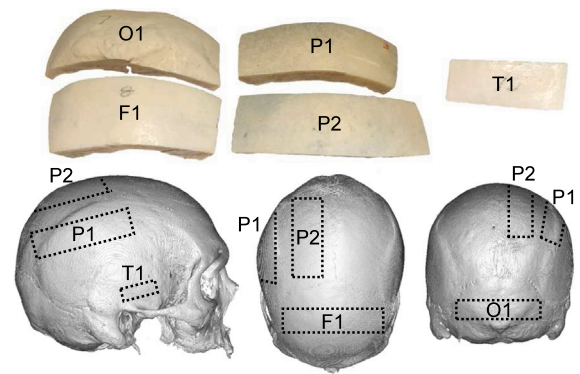

Fig. 1. The skull segments considered in this study and their approximate locations on the human skull.

micro-computed tomographic (μCT) scan images of a bone segment are obtained from an 87-year-old human skull specimen of unknown race and medical history using Scanco Medical μCT 50 scanner at 49.6 μm resolution. These images are then used in a model construction algorithm built using MATLAB's image processing toolbox (Anon, 2020). The algorithm begins by identifying the outline of the skull segment, from which the inner and outer boundaries are isolated using corner coordinates. The boundaries are then divided into uniformly-spaced sets of points. From each point on a boundary, the algorithm marches towards the opposite side until a gray scale value below threshold is encountered, indicating that the coordinates correspond to a cortical table–diploë boundary. The algorithm proceeds until each point on the inner and outer boundaries is matched to a corresponding point on a cortical table–diploë boundary. The matched points are then filtered to attenuate local noise using a Savitzky–Golay filter (Orfanidis, 1995) that fits subsets of adjacent points to a second order polynomial, generating two smooth curves that separate the diploë and the cortical tables. Note that for even finer resolution (near 10 μm and finer) images, pores in the cortical tables are distinct as observed in Alexander et al. (2019) and would distort the diploë boundary identification. The resolution of such image sets can be reduced for use with this method. On the other hand, the algorithm does not detect small diploë pores that appear homogeneous in lower resolution images. The employed 49.6 μm resolution strikes a balance between these two considerations, yielding a visually reasonable separation between the bone regions as seen in Fig. 2. Alternatively, a porosity percentage-based diploë boundary identification described in Alexander et al. (2019) could be employed to avoid the aforementioned porosity considerations.

The described boundary identification procedure is repeated for each scan image. The identified overall outline of the bone segment, as well as the cortical table–diploë boundary coordinates are then imported into COMSOL Multiphysics 5.5 (Comsol Multiphysics 5.5, 2020). The overall closed outline of the bone segment is lofted using COMSOL design module to generate the solid geometry, whereas the open cortical table–diploë boundaries are lofted to create two surfaces that divide the solid into three distinct layers: the inner cortical table, the diploë, and the outer cortical table. A comparison between a bone sample and its finished numerical model is shown in Fig. 3. It should be noted that in reality the exact point at which the diploë begins and a cortical table ends is ill-defined. For this reason, the gray scale threshold and the number of points in each Savitzky–Golay filter subset (typically 15%–25% of boundary points) are adjusted until a visually reasonable layer separation is realized. The same options are then used for all CT-scan images for a given skull segment. Numerical models are constructed for each of the five skull segments in Fig. 1 using CT-scan images of bone segments extracted from the frontal, occipital, parietal and temporal bones.
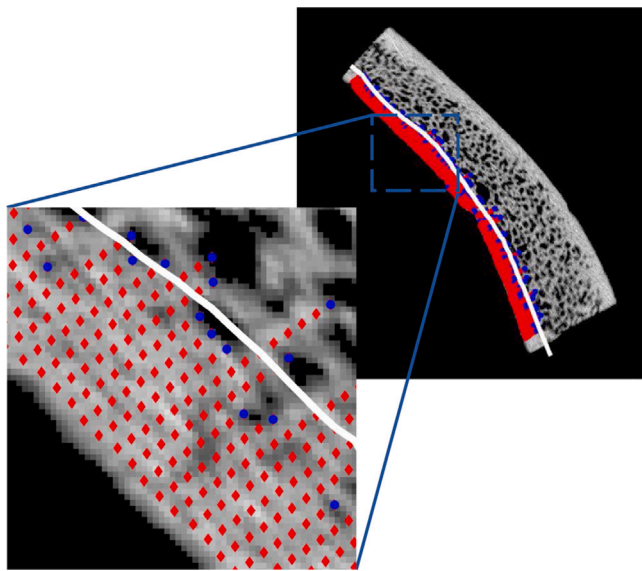
Fig. 2. Inner cortical table–diploë boundary identification on a sample scan image of bone segment P2. Red diamonds are marching steps, filled blue circles are identified points on the boundary, and the white solid line is the filtered boundary.
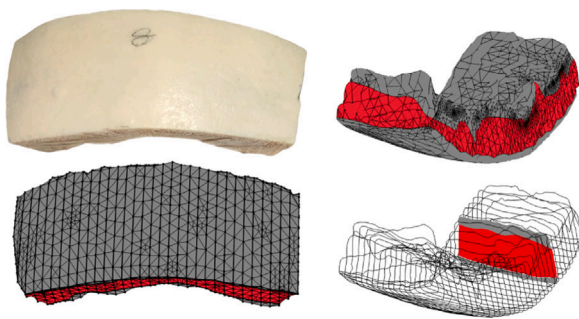

Fig. 3. Skull segment F1 and its corresponding finite element mesh including a wireframe image where the layers are better observed.

The numerical model construction procedure captures the cortical table and diploë separation well in particular for regular bone geometries with well-defined diploë and cortical tables. The parietal segment geometries illustrate this point well; in Fig. 4, the outer surfaces of the P1 segment are smooth, which results in a finished numerical model in which the cortical tables and the diploë are faithfully captured. More complex surfaces such as that in the left F1 image are not captured as intricately because of local cortical bone growths separated from the main cortical layer, causing the local identified cortical table–diploë boundary to reside between the cortical bone growth and the outer cortical table. On the other hand, most of the F1 geometry is closer to the more regular right image, making the inconsistencies in the identified cortical table–diploë boundary for the left image local noise that is relatively inconsequential in the overall layer separation in the finished numerical model. It should be noted that in many areas of the diploë, the porosity is not uniform. For example, there is a large diploic channel in the middle of the right P1 image. The right F1 image, on the other hand, exhibits significant variation in local diploë mass density, with higher bone densities observed in the top-left area of the diploë. All such non-uniformities are homogenized into the middle layer of the numerical model.

3. Experimental procedure

The goal of the experiments is to identify modal frequencies, damping ratios, and mode shapes of the bone segments. Due to their irregular
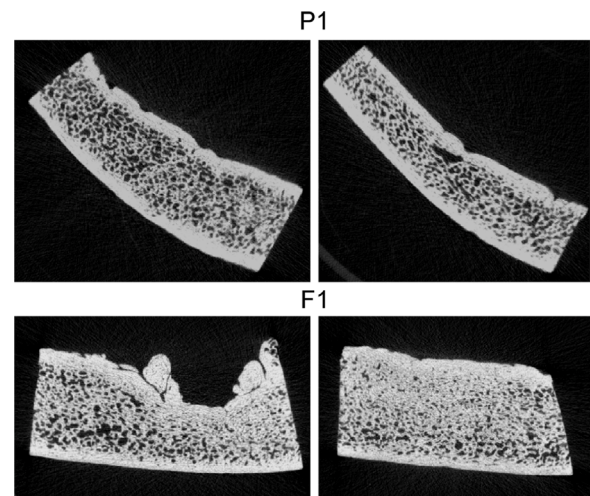

Fig. 4. Sample μCT scans of the P1 (top) and F1 (bottom) skull segments.

shape, bone segments are difficult to secure to a shaker for base excitation. Additionally, because the skull segments are light structures, mass loading from a stinger would impact the vibrational behavior. For the aforementioned reasons, a speaker was used to acoustically excite the structure placed on foam to emulate free boundary conditions, thus avoiding the problems of clamping and added mass. This approach comes with the compromise that the excitation pressure can vary locally on the bone surface because the segments are asymmetrically placed in the speaker's near-field to improve excitation of asymmetric modes and to maximize the signal-to-noise ratio.

The schematic of the experimental setup is shown in Fig. 5. Using a signal generator with data acquisition system and software included in the scanning laser Doppler vibrometer (Polytec PSV-500) system, a noise burst with frequency content in the auditory range is sent to a speaker (Klipsch RP-400M) through a power amplifier (QSC PLX1602). The velocity measurement is triggered internally and is obtained at approximately 100 points with the scanning laser Doppler vibrometer using 10 averages. The laser software automatically converts the time-domain measurements into FRFs, which evaluate a transfer function between the surface velocity and the excitation voltage signal. The FRFs are then converted from velocity/voltage to velocity/pressure using the free field pressure measured with a microphone at the location of the bone segment. A sample FRF is reported in Fig. 6 where the mode shapes corresponding to the most prominent resonance peaks are also shown. These mode shapes are used in the parameter identification scheme described in the following section. Lastly, it is noted that retroreflective tape is used on the bone surface to improve the laser signal-to-noise-ratio. However, due to the surface imperfections of the bone, at certain measurement points the tape adheres poorly. For this reason, measurement points with coherence values less than 0.95 are excluded from the mode shape construction. After the removal of noisy measurement points, on average more than 80 points remain for evaluation of the experimental mode shapes, which is sufficient to capture the first handful of bone segment modes as seen in Fig. 6.

4. Parameter identification

The considered modal frequencies were observed to exhibit insensitivity to Poisson's ratio. For this reason, in the parameter identification analyses, the Poisson's ratio of the cortical tables and the diploë is assumed to be a constant parameter in similar vein to other modal frequency-based parameter identification efforts in bone (Taylor et al., 2002). The Poisson's ratios are set to $v_c = 0.25$ and $v_d = 0.10$ in close accordance with those used in the literature (see, e.g. Chang et al., 2016; Sahoo et al., 2013).
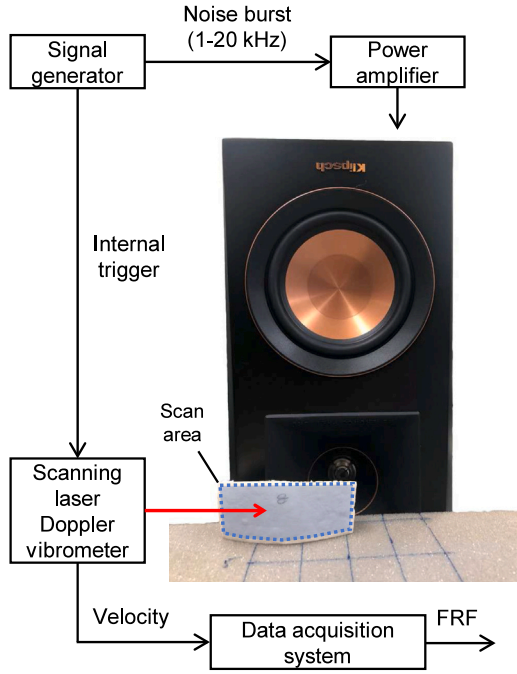
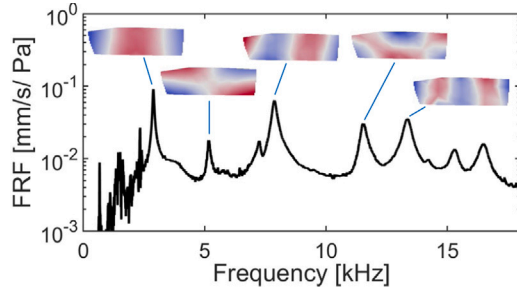**Fig. 5.** The experimental setup with segment F1 shown.

Fig. 6. The average FRF across all measurement points for a sample skull segment (P2). The experimental mode shapes used in the parameter identification scheme are shown.

4.1. Mass density evaluation

The cortical and diploë mass densities ρ_c and ρ_d of a given skull segment are calculated using an expression equating the total measured bone mass to the total numerical mass estimated for the cortical and diploë layers reconstructed using the procedure outlined in Section 2. Additionally, because mass density is linearly proportional to Hounsfield Unit (HU) in the μCT-scans, the ratio between the cortical and diploë mass densities is linearly related to the corresponding average HU ratio (HU_c/HU_d) in the bone regions. The expressions for equal numerical and experimental mass, and for the linear relation between mass density and HU are stated as

$$\rho_c V_c + \rho_d V_d = m_{exp}, \tag{1}$$

$$\rho_c/\rho_d = HU_c/HU_d, \tag{2}$$

where $V_{c,d}$ are the numerically reconstructed cortical and diploë volumes, and m_{exp} is the measured total mass of the bone segment. Eqs. (1) and (2) are solved for ρ_c and ρ_d directly.

4.2. Elastic modulus estimation

With the assumed values of the Poisson's ratio and the mass density parameters computed as in Section 4.1, the identification of the equivalent Young's modulus of the cortical bone (E_c) and the diploë (E_d) bone is carried out by applying the methodology described in Mazzotti et al. (2019), which is based on a regularized Gauss–Newton method, and which was applied for the identification of the orthotropic and equivalent isotropic elastic constants of parietal bones using Lamb waves (Mazzotti et al., 2020; Mazzotti et al., 2021b,c). For a given set of nominal values $\mathbf{E}_0 = \{E_{c0}, E_{d0}\}^{\mathrm{T}}$, the method reconstructs the optimal Young's moduli $\mathbf{E} = \{E_c, E_d\}^{\mathrm{T}}$ as $\mathbf{E} = \mathbf{a}^{\mathrm{T}}\mathbf{E}_0$, where $\mathbf{a} = \{a_1, a_2\}^{\mathrm{T}}$ is an unknown set of $N_a = 2$ dimensionless scaling coefficients such that $\mathbf{a} \in \mathbb{R}^{N_a}_{[0,1]}$. This set is retrieved from the iterative sequence $\mathbf{a}_{k+1} = \mathbf{a}_k + \delta\mathbf{a}_k$ by minimizing the bound constrained trust-region quadratic problem

$$\min_{\delta\mathbf{a}_k \in \mathbb{R}^{N_a}_{[0,1]} - \{\mathbf{0}\}} \left\{ (\nabla_{\mathbf{a}}\mathcal{F}(\mathbf{a}_k))^{\mathrm{T}}\delta\mathbf{a}_{k-1} + \frac{1}{2}\delta\mathbf{a}_k^{\mathrm{T}}\nabla_{\mathbf{a}}^2\mathcal{F}(\mathbf{a}_k)\delta\mathbf{a}_{k-1} \right\},$$

subjected to $\quad \mathbf{l} - \mathbf{a}_k \leq \delta\mathbf{a}_k \leq \mathbf{u} - \mathbf{a}_k,$

and the trust region constraint $\quad \|\delta\mathbf{a}_k\|_{\infty} \leq \Delta_k,$

$$\tag{3}$$

where $\mathbf{l}$ and $\mathbf{u}$ denote physically admissible lower and upper bounds for the Youngs' moduli, Δ_k indicates the maximum size of the trust region hyperbox in $\mathbb{R}^{N_a}_{[0,1]}$ and

$$\mathcal{F}(\mathbf{a}_k) = \frac{1}{2}\beta\|\mathbf{r}(\mathbf{a}_k)\|_2^2 \left(\|\delta\mathbf{a}_{k-1}\|_2^2 + N_a\Delta_{k-1} \right) \tag{4}$$

is a multiplicative regularized functional in which $\beta = 2/(N_\omega N_a \Delta_{k-1})$, $\delta\mathbf{a}_{k-1} = \mathbf{a}_k - \mathbf{a}_{k-1}$, while

$$\mathbf{r}(\mathbf{a}_k) = \{.., \omega_i^2(\mathbf{a}_k)/\tilde{\omega}_i^2 - 1, ..\}^{\mathrm{T}} \tag{5}$$

represents the data misfit to be minimized. In Eq. (5), $\tilde{\omega}_i^2$ ($i = 1, \ldots, N_\omega$) indicates the ith experimental natural frequency while $\omega_i(\mathbf{a}_k)$ denotes its corresponding numerical counterpart obtained from the eigenvalue problem

$$\left[\mathbf{K}(\mathbf{E}(\mathbf{a}_k)) - \omega^2\mathbf{M} \right] \mathbf{Q} = \mathbf{0} \tag{6}$$

for the current solution $\mathbf{a}_k$. In this work, Eq. (6) is solved via COMSOL Multiphysics 5.5 (Comsol Multiphysics 5.5, 2020), while the pairing between the numerical frequencies $\omega_j(\mathbf{a}_k)$ and the corresponding experimental ones $\tilde{\omega}_j$ is performed by means of the Modal Assurance Criterion (MAC) (Pastor et al., 2012), which measures the spatial similarity between two mode shapes. The MAC value ranges between zero and one, with high MAC values corresponding to high similarity. The gradient vector $\nabla_{\mathbf{a}}\mathcal{F}(\mathbf{a}_k)$ and Hessian matrix $\nabla_{\mathbf{a}}^2\mathcal{F}(\mathbf{a}_k)$ can be derived from Eqs. (3) and (6) as

$$\nabla_{\mathbf{a}}\mathcal{F}(\mathbf{a}_k) = \beta \left(\|\delta\mathbf{a}_{k-1}\|_2^2 + \Delta_{k-1} \right) \mathbf{J}^{\mathrm{T}}(\mathbf{a}_k)\mathbf{r}(\mathbf{a}_k) + \beta\|\mathbf{r}(\mathbf{a}_k)\|_2^2\delta\mathbf{a}_{k-1}, \tag{7}$$

$$\begin{aligned}\nabla_{\mathbf{a}}^2\mathcal{F}(\mathbf{a}_k) = &\beta \left(\|\delta\mathbf{a}_{k-1}\|_2^2 + \Delta_{k-1} \right) \mathbf{J}^{\mathrm{T}}(\mathbf{a}_k)\mathbf{J}(\mathbf{a}_k) \\ &+ \beta\|\mathbf{r}(\mathbf{a}_k)\|_2^2\mathbf{I} \\ &+ 2\beta[\mathbf{J}^{\mathrm{T}}(\mathbf{a}_k)\mathbf{r}(\mathbf{a}_k)] \otimes \delta\mathbf{a}_{k-1} \\ &+ 2\beta\delta\mathbf{a}_{k-1} \otimes [\mathbf{J}^{\mathrm{T}}(\mathbf{a}_k)\mathbf{r}(\mathbf{a}_k)],\end{aligned} \tag{8}$$

in which $\mathbf{J}(\mathbf{a}_k) = [\partial\mathbf{r}(\mathbf{a})/\partial\mathbf{a}]_{\mathbf{a}=\mathbf{a}_k}$ represents the Jacobian of the residuals. The (i, j)th component of $\mathbf{J}(\mathbf{a}_k)$ corresponds to the derivative of the ith natural frequency calculated with respect to the jth dimensionless parameter. Using Eqs. (5) and (6), one obtains

$$[\mathbf{J}(\mathbf{a}_k)]_{ij} = \frac{1}{\tilde{\omega}_i^2} \frac{\mathbf{Q}^{\mathrm{T}}(\mathbf{a}_k) \left[\partial\mathbf{K}(\mathbf{a})/\partial a_j \right]_{\mathbf{a}=\mathbf{a}_k} \mathbf{Q}(\mathbf{a}_k)}{\mathbf{Q}^{\mathrm{T}}(\mathbf{a}_k)\mathbf{M}(\mathbf{a}_k)\mathbf{Q}(\mathbf{a}_k)}. \tag{9}$$

The last step necessary to calculate the update $\delta\mathbf{a}_k$ in Eq. (3) is to determine the Δ_k such that the quadratic problem is guaranteed to have a unique solution for low to moderate levels of noise in $\tilde{\omega}_j$. Following the analysis in Mazzotti et al. (2019), this parameter can be
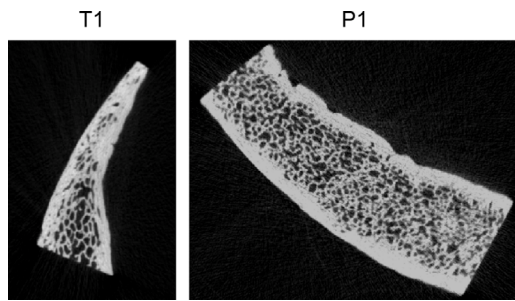
T1   P1

Fig. 7. μCT scans of the T1 and P1 segments.

computed as $\Delta_k = [-d_2 + (d_2^2 - 4d_1d_3)^{1/2}]/(2d_1)$, in which $d_1 = N_a^2$, $d_2 = 2\mathrm{sgn}(\delta\mathbf{a}_{k-1})^{\mathrm{T}}\delta\mathbf{a}_{k-1}$, $d_3 = 2\|\delta\mathbf{a}_{k-1}\|_2^2 - 2N_a\Delta_{k-1}$. Once the maximum size of the trust region Δ_k and Eqs. (7) and (8) have been evaluated, the quadratic problem (3) can be solved using the trust region reflective (TRR) algorithm described in Coleman and Li (1996) and Branch et al. (1999).

5. Results

The material properties including the identified mass densities and Young's moduli obtained from the parameter identification scheme are shown in Table 1 for each cranial bone region. The cortical Young's moduli range between 14.17 and 18.73 GPa, the diploë Young's moduli between 2.43 and 6.15 GPa, the cortical mass densities between 1926 and 2165 kg/m^3, and the diploë mass densities between 920 and 1290 kg/m^3. The cortical mass densities are consistently slightly higher (8%–14% depending on bone region) than those reported in the literature (Peterson and Dechow, 2003). It is worth noting that the diploë mass density of T1 is low compared to other bone segments, which is explained by significantly larger pores. The difference in pore size is clearly seen in Fig. 7, in which a representative μCT scan of the T1 segment is shown next to one from the P1 segment using the same length scale. The isotropic cortical Young's moduli here fall between the lower and upper bounds of the orthotropic Young's moduli reported in Peterson and Dechow (2003). The literature on the material properties of the diploë are scarce, with only the properties of fresh parietal and frontal bone being reported (Alexander et al., 2020), limiting the available elastic properties for comparison. The diploë Young's moduli here are higher (for frontal bone, 5.0 GPa as opposed to 2.6 GPa), likely due to the bone samples being dry whereas those used in Alexander et al. (2020) are fresh.

The converged numerical natural frequencies and mode shapes are obtained using the material properties in Table 1. These modal frequencies are listed along with the experimental ones, their error, the experimental damping ratio, and the MAC values in Table 2. Note that the error in modal frequency is less than 5% for all modes, with the largest errors observed for the F1 segment, likely due to local irregularities in its geometry as discussed in Section 2 with reference to Fig. 4. The damping ratios are extracted using the classical half-power point method (Inman, 1994) and are on the order of 2%, which are in agreement with the values found in other works for skull bone (Horácek et al., 2003; Eslaminejad et al., 2020). No significant difference in damping ratios is observed depending on the skull segment. For the $m1$ modes, the damping ratio remains remarkably consistent from sample to sample at 1.6% to 1.7%. It is noted that the damping ratio for mode O1-$m4$ is not reported since it could not be reliably extracted.

For most modes, the MAC values are above 0.9, although some higher frequency modes exhibit lower MAC values. This is likely because high order modes (with shorter wavelengths) are more localized, making the MAC values more sensitive to the coordinate matching between the experimental and numerical modes and to local perturbations in the material properties and geometry, which are assumed as

Table 1
The material properties obtained from parameter identification for each of the five skull segments.

Skull Segment	E_c [GPa]	E_d [GPa]	ρ_c [kg/m^3]	ρ_d [kg/m^3]
P1	18.73	4.35	2165	1237
P2	14.70	5.70	1944	1211
F1	14.17	5.00	1926	1246
O1	15.35	6.15	2048	1290
T1	15.45	2.43	2044	920

Table 2
The modal frequencies and error in the numerical results, experimental damping ratios for each mode used in the parameter identification process, and MAC values.

Skull Segment	Mode ID	f_{exp}[Hz]	f_{num}[Hz]	Error [%]	ζ[%]	MAC
	m1	3484	3452	0.9	1.7	0.986
	m2	5109	5242	2.6	1.8	0.996
P1	m3	8097	7959	1.7	1.9	0.916
	m4	10825	10848	0.2	1.8	0.948
	m5	14597	14540	0.4	2.1	0.928
	m1	2891	2913	0.8	1.6	0.976
	m2	5159	5193	0.7	2.2	0.937
P2	m3	7872	7822	0.6	2.0	0.969
	m4	11519	11472	0.4	1.9	0.958
	m5	13359	13321	0.3	2.0	0.923
	m1	3656	3807	4.1	1.6	0.988
	m2	5747	5729	0.3	1.9	0.987
F1	m3	8853	8653	2.2	2.2	0.896
	m4	10725	11070	3.2	1.8	0.966
	m5	15909	15158	4.7	2.6	0.550
	m1	3134	3226	3.0	1.7	0.950
	m2	5150	5074	1.4	2.2	0.979
O1	m3	6863	6780	1.3	2.0	0.970
	m4	8409	8395	0.2	N/A	0.900
	m5	12341	12295	0.4	2.9	0.838
	m1	5778	5778	0.0	1.6	0.965
T1	m2	7838	7838	0.0	2.5	0.871
	m3	14806	14806	0.0	2.2	0.829

homogeneous through each layer in the numerical model. The full MAC matrices are displayed in Fig. 8. Note that in all MAC matrices except for T1, the experimental and numerical mode numbers do not agree past a certain mode. This is because weakly excited experimental modes are excluded from the analysis, which results in an offset between the experimental and numerical mode numbers. The experimental and numerical mode shapes with the converged material properties are shown in Figs. 9–13. The mode shapes bear similarities with beam and plate modes, with, for example, the first bending mode of a free–free beam being a clear analogue to the $m1$ mode of each skull segment. Higher modes are more distinct from their plate and beam counterparts as the complex bone geometry has more influence on the modes at higher frequencies.

Finally, for reference, the elastic parameters obtained using a single layer approximation of the bone are shown in Table 3 assuming $v = 0.25$. The single layer elastic moduli and mass densities fall between those reported for the diploë and the cortical bone in Table 1 as expected. The results for mass density are within the ranges reported in the literature (McElhaney et al., 1970). The modulus, however, displays large variation in the literature. For example, the reported moduli range from relatively low (2.4 GPa $\pm$ 1.4 GPa in McElhaney et al., 1970 and 3.3 GPa in Alexander et al., 2020) to very high (7.46 $\pm$ 5.39 GPa to 15.54 GPa $\pm$ 10.29 GPa at extreme ends of tested strain rates in Motherway et al., 2009), making meaningful comparison challenging. The average error in natural frequencies across the considered modes in the given frequency range for the single layer model is 2.3%, which is slightly higher than that observed for the three layer model (1.3%). While a single layer model might be acceptable at
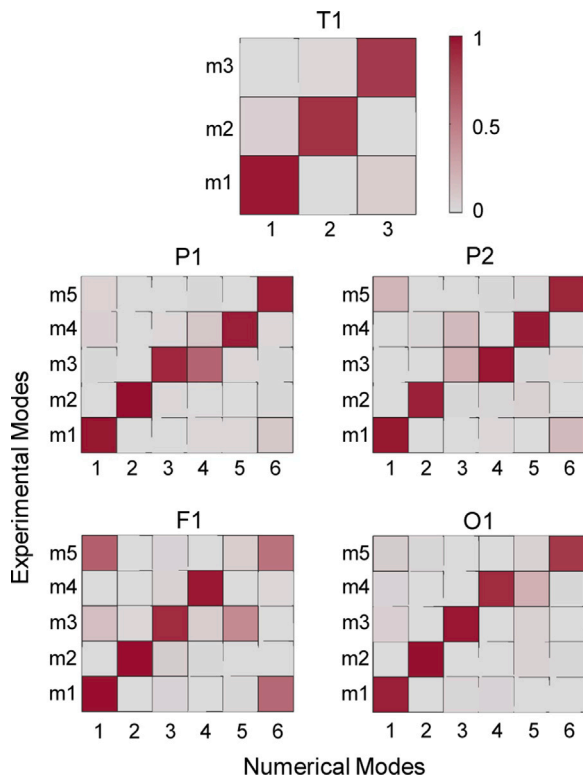
Fig. 8. The MAC matrices between the experimental modes and the numerical modes using the identified elastic parameters.
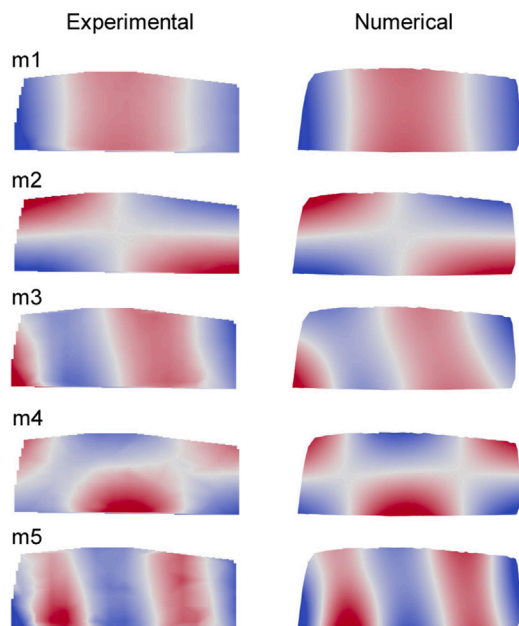

Fig. 9. Experimental and numerical mode shapes of P1 used in the parameter identification scheme. Animations available as supplementary files.
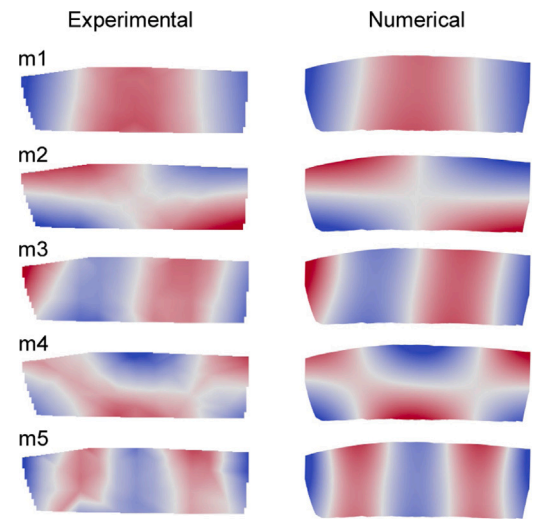

Fig. 10. Experimental and numerical mode shapes of P2 used in the parameter identification scheme. Animations available as supplementary files.
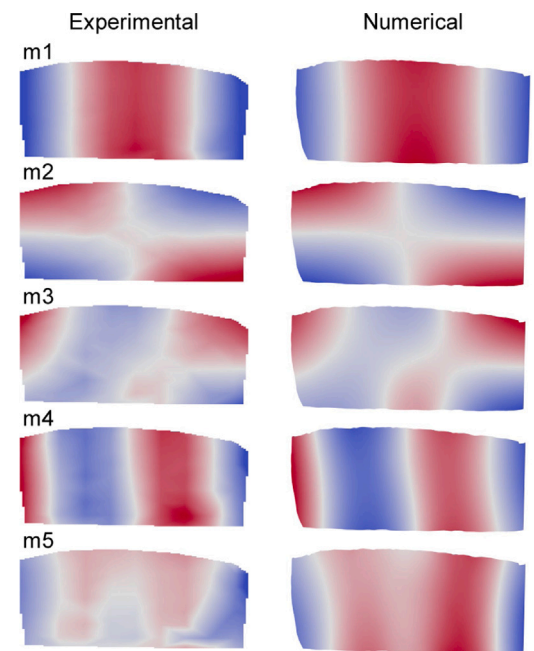

Fig. 11. Experimental and numerical mode shapes of F1 used in the parameter identification scheme. Animations available as supplementary files.

low frequencies for certain applications, head models featuring separate cortical tables and diploë are frequently employed (Kleiven and von Holst, 2002; Sahoo et al., 2013; Kang et al., 1997; Cotton et al., 2016). Furthermore, higher frequencies used in the emerging field of guided waves and mode conversion for medical ultrasound require layered modeling as bone porosity and layeredness become more important at shorter wavelengths (Mazzotti et al., 2020; Mazzotti et al., 2021b). We

have recently demonstrated the use of the identified elastic parameters from the three-layered modeling framework given here in the context of guided cranial wave radiation into an adjacent fluid medium (Mazzotti et al., 2021a; Kohtanen et al., 2021a,b).

6. Conclusions

In this work, a process for constructing layered finite element models with separate domains for the cortical tables and the diploë is developed. The geometry is reconstructed from micro-computed tomographic scan (μCT) images of cranial bone segments. The reconstruction process is applied to generate models for five bone segments extracted
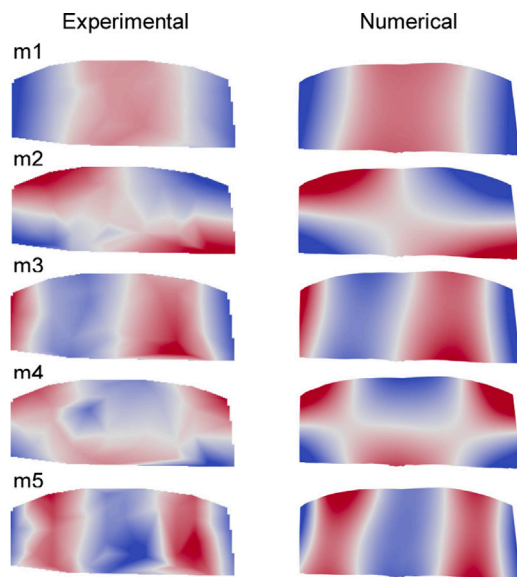
Fig. 12. Experimental and numerical mode shapes of O1 used in the parameter identification scheme. Animations available as supplementary files.
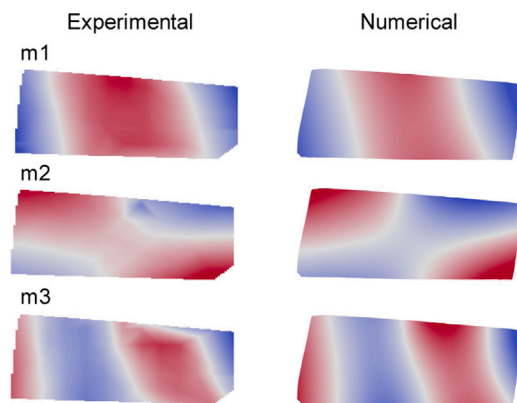

Fig. 13. Experimental and numerical mode shapes of T1 used in the parameter identification scheme. Animations available as supplementary files.

Table 3
The single layer material properties for each of the five skull segments.

Skull Segment	E [GPa]	ρ [kg/m^3]
P1	10.66	1482
P2	10.76	1478
F1	9.36	1510
O1	11.94	1673
T1	11.50	1669

from the four largest cranial bones (parietal, frontal, occipital, and temporal). Vibration experiments using an acoustic excitation source are conducted to obtain experimental modal frequencies and mode shapes. The elastic parameters in the numerical models are then optimized in a parameter identification scheme, yielding Young's moduli for the cortical bone and the diploë that provide optimum agreement between the experiment and numerical results. The Young's moduli reported for the diploë are some of the only such results in the literature.

With the identified elastic parameters and mass densities from μCT-scan images and experimental mass, the experimental and numerical mode shapes are in general excellent agreement with average MAC values above 0.90. The corresponding modal frequencies have a mean error of 1.3% across all the bone segments. Higher but reasonable errors

are observed for more irregular bone segments such as F1 and O1 for which the model construction scheme is not as well-suited. These fundamental vibration results serve as a tool to validate the use of three layer cranial bone models for studies of the human skull or head in the audio frequency regime.

The bone segments used in this study were intentionally extracted without the inclusion of sutures. The authors hypothesize that sutures can in many cases have a profound effect on the vibrational behavior of cranial bone. Further analysis will investigate such effects for which a layered model with homogenized sutures will likely not be sufficient by itself.

Finally, the framework and results presented here are useful not only for basic mechanics and vibration investigations for the human head/skull, but also for the growing field of transcranial ultrasound using Lamb waves and mode conversion (Firouzi et al., 2017; Estrada et al., 2018; Sugino et al., 2021; Mazzotti et al., 2021b,c; Kohtanen et al., 2021a,b), in which accurate representation of the elastic properties of the diploë and cortical tables is indispensable.

CRediT authorship contribution statement

E. Kohtanen: Formal analysis, Methodology, Investigation, Software, Data curation, Writing – original draft. **M. Mazzotti:** Formal analysis, software, Writing – original draft. **M. Ruzzene:** Conceptualization, Funding acquisition, Supervision, Writing – review & editing. **A. Erturk:** Conceptualization, Methodology, Funding acquisition, Supervision, Writing – review & editing.

Declaration of competing interest

The authors declare that they have no known competing financial interests or personal relationships that could have appeared to influence the work reported in this paper.

Funding

Appendix A. Supplementary data

Supplementary material related to this article can be found online at https://doi.org/10.1016/j.jmbbm.2021.104747.

References

Alexander, S.L., Gunnarsson, C.A., Rafaels, K., Weerasooriya, T., 2020. Multiscale response of the human skull to quasi-static compression. J. Mech. Behav. Biomed. Mater. 102, 103492.

Alexander, S.L., Rafaels, K., Gunnarsson, C.A., Weerasooriya, T., 2019. Structural analysis of the frontal and parietal bones of the human skull. J. Mech. Behav. Biomed. Mater. 90, 689–701.

Anon, 2020. MATLAB Version 9.8.0.1451342 (R2020a). The Mathworks, Inc., Natick, Massachusetts.

Branch, M., Coleman, T., Li, Y., 1999. A subspace, interior, and conjugate gradient method for large-scale bound-constrained minimization problems. SIAM J. Sci. Comput. 21 (1), 1–23. http://dx.doi.org/10.1137/S1064827595289108.

Chang, Y., Kim, N., Stenfelt, S., 2016. The development of a whole-head human finite-element model for simulation of the transmission of bone-conducted sound. J. Acoust. Soc. Am. 140 (3), 1635–1651.

Charalambopoulos, A., Dassios, G., Fotiadis, D., Massalas, C., 1997. Frequency spectrum of the human head-neck system. Internat. J. Engrg. Sci. 35 (8), 753–768.

Coleman, T., Li, Y., 1996. An Interior Trust Region approach for nonlinear minimization subject to bounds. SIAM J. Optim. 6 (2), 418–445. http://dx.doi.org/10.1137/0806023.

Comsol Multiphysics 5.5, 2020. URL: https://www.comsol.com/.

Cotton, R., Pearce, C.W., Young, P.G., Kota, N., Leung, A., Bagchi, A., Qidwai, S., 2016. Development of a geometrically accurate and adaptable finite element head model for impact simulation: the Naval Research Laboratory–Simpleware Head Model. Comput. Methods Biomech. Biomed. Eng. 19 (1), 101–113.

El Baroudi, A., Razafimahery, F., Rakotomanana-Ravelonarivo, L., 2012. Three-dimensional modal analysis of an idealized human head including fluid–structure interaction effects. Acta Mech. 223 (9), 1899–1915.

Engin, A.E., 1969. The axisymmetric response of a fluid-filled spherical shell to a local radial impulse—a model for head injury. J. Biomech. 2 (3), 325–341.

Eslaminejad, A., Hosseini-Farid, M., Ziejewski, M., Karami, G., 2020. Constitutive properties determination of human cranium by an experimental–computational modal analysis. J. Vib. Acoust. 142 (1).

Estrada, H., Gottschalk, S., Reiss, M., Neuschmelting, V., Goldbrunner, R., Razansky, D., 2018. Observation of guided acoustic waves in a human skull. Ultrasound Med. Biol. 44 (11), 2388–2392.

Firouzi, K., Ghanouni, P., Khuri-Yakub, B.T., 2017. Efficient transcranial ultrasound delivery via excitation of lamb waves: Concept and preliminary results. In: 2017 IEEE International Ultrasonics Symposium. IUS, IEEE, pp. 1–4.

Franke, E.K., 1956. Response of the human skull to mechanical vibrations. J. Acoust. Soc. Am. 28 (6), 1277–1284.

Håkansson, B., Brandt, A., Carlsson, P., Tjellström, A., 1994. Resonance frequencies of the human skull in vivo. J. Acoust. Soc. Am. 95 (3), 1474–1481.

Hickling, R., Wenner, M.L., 1973. Mathematical model of a head subjected to an axisymmetric impact. J. Biomech. 6 (2), 115–132.

Hodgson, V., Gurdjian, E., Thomas, L., 1967. The Determination of Response Characteristics of the Head with Emphasis on Mechanical Impedance Techniques. Technical Report, SAE Technical Paper.

Horácek, J., Veselỳ, J., Pešek, L., Vohradník, M., 2003. Fundamental dynamic characteristics of human skull. In: Nat. Conf. Engineering Mechanics. pp. 12–15.

Inman, D.J., 1994. Engineering Vibration, Vol. 3. Prentice Hall Englewood Cliffs, NJ.

Kang, H.-S., Willinger, R., Diaw, B.M., Chinn, B., 1997. Validation of a 3D anatomic human head model and replication of head impact in motorcycle accident by finite element modeling. SAE Trans. 3849–3858.

Khalil, T.B., Viano, D., Smith, D., 1979. Experimental analysis of the vibrational characteristics of the human skull. J. Sound Vib. 63 (3), 351–376.

Kleiven, S., von Holst, H., 2002. Consequences of head size following trauma to the human head. J. Biomech. 35 (2), 153–160.

Kohtanen, E., Mazzotti, M., Ruzzene, M., Erturk, A., 2021a. Transcranial radiation characteristics of leaky lamb waves in different regions of a human skull. In: Proceedings of Meetings on Acoustics, Vol. 149. (4), p. A18. http://dx.doi.org/10.1121/10.0004390.

Kohtanen, E., Mazzotti, M., Ruzzene, M., Erturk, A., 2021b. Leveraging vibrations and guided waves in a human skull. In: ASME International Mechanical Engineering Congress and Exposition (accepted).

Laksari, K., Kurt, M., Babaee, H., Kleiven, S., Camarillo, D., 2018. Mechanistic insights into human brain impact dynamics through modal analysis. Phys. Rev. Lett. 120 (13), 138101.

Mazzotti, M., Kohtanen, E., Erturk, A., Ruzzene, M., 2021a. Radiation characteristics of cranial leaky lamb waves. IEEE Trans. Ultrason. Ferroelectr. Freq. Control 68 (6), 2129–2140.

Mazzotti, M., Kohtanen, E., Erturk, A., Ruzzene, M., 2021c. Experimental and numerical analysis of Lamb wave transmission through the coronal suture of a dry human skull. In: Proceedings of Meetings on Acoustics, Vol. 149. (4), p. A42. http://dx.doi.org/10.1121/10.0004462.

Mazzotti, M., Mao, Q., Bartoli, I., Livadiotis, S., 2019. A multiplicative regularized Gauss-Newton method with trust region Sequential Quadratic Programming for structural model updating. Mech. Syst. Signal Process. 131, 417–433. http://dx.doi.org/10.1016/j.ymssp.2019.05.062.

Mazzotti, M., Sugino, C., Erturk, A., Ruzzene, M., 2020. Matrix pencil estimation of guided waves dispersion in a human skull. In: 2020 IEEE International Ultrasonics Symposium. IUS, pp. 1–3. http://dx.doi.org/10.1109/IUS46767.2020.9251282.

Mazzotti, M., Sugino, C., Kohtanen, E., Erturk, A., Ruzzene, M., 2021b. Experimental identification of high order Lamb waves and estimation of the mechanical properties of a dry human skull. Ultrasonics 113, 106343. http://dx.doi.org/10.1016/j.ultras.2020.106343.

McElhaney, J.H., Fogle, J.L., Melvin, J.W., Haynes, R.R., Roberts, V.L., Alem, N.M., 1970. Mechanical properties of cranial bone. J. Biomech. 3 (5), 495–511.

McKnight, C.L., Doman, D.A., Brown, J.A., Bance, M., Adamson, R.B., 2013. Direct measurement of the wavelength of sound waves in the human skull. J. Acoust. Soc. Am. 133 (1), 136–145.

Motherway, J.A., Verschueren, P., Van der Perre, G., Vander Sloten, J., Gilchrist, M.D., 2009. The mechanical properties of cranial bone: the effect of loading rate and cranial sampling position. J. Biomech. 42 (13), 2129–2135.

Nickell, R., Marcal, P., 1974. In-Vacuo modal dynamic response of the human skull. J. Eng. Ind.

Orfanidis, S.J., 1995. Introduction To Signal Processing. Prentice-Hall, Inc..

Pastor, M., Binda, M., Harčarik, T., 2012. Modal assurance criterion. Procedia Eng. 48, 543–548. http://dx.doi.org/10.1016/j.proeng.2012.09.551, Modelling of Mechanical and Mechatronics Systems.

Peterson, J., Dechow, P.C., 2003. Material properties of the human cranial vault and zygoma. Anat. Rec. A 274 (1), 785–797.

Sahoo, D., Deck, C., Yoganandan, N., Willinger, R., 2013. Anisotropic composite human skull model and skull fracture validation against temporo-parietal skull fracture. J. Mech. Behav. Biomed. Mater. 28, 340–353.

Stalnaker, R.L., Fogle, J.L., McElhaney, J.H., 1971. Driving point impedance characteristics of the head. J. Biomech. 4 (2), 127–139.

Sugino, C., Ruzzene, M., Erturk, A., 2021. Experimental and computational investigation of guided waves in a human skull. Ultrasound Med. Biol. 47 (3), 787–798.

Taylor, W., Roland, E., Ploeg, H., Hertig, D., Klabunde, R., Warner, M., Hobatho, M., Rakotomanana, L., Clift, S., 2002. Determination of orthotropic bone elastic constants using FEA and modal analysis. J. Biomech. 35 (6), 767–773.

Tse, K.M., Tan, L.B., Lee, H.P., 2017. The skull and brain: Computer models for the head and its protection. In: Military Injury Biomechanics. CRC Press, pp. 175–220.

Tse, K.M., Tan, L.B., Lim, S.P., Lee, H.P., 2015. Conventional and complex modal analyses of a finite element model of human head and neck. Comput. Methods Biomech. Biomed. Eng. 18 (9), 961–973.

Voo, L., Kumaresan, S., Pintar, F.A., Yoganandan, N., Sances, A., 1996. Finite-element models of the human head. Med. Biol. Eng. Comput. 34 (5), 375–381.